Applied Physics A (2022) 128:950
https://doi.org/10.1007/s00339-022-06021-x

Applied Physics A
Materials Science & Processing

S.I. : COLA 2021/2022

$CsPbBr_3$ deposited by laser ablation: effects of post-growth aging, oxygen adsorption and annealing on film properties

Maura Cesaria[1] · Gianluca Quarta[2,3] · Maria Rachele Guascito[4] · Marco Mazzeo[1] · Marcella Marra[1,3] · Chiara Provenzano[3,4,5] · Muhammad Rizwan Aziz[1] · Maurizio Martino[1,3] · Lucio Calcagnile[2,3] · Anna Paola Caricato[1,3]

Received: 31 May 2022 / Accepted: 17 August 2022 / Published online: 5 October 2022

Abstract
All-inorganic perovskites are widely investigated as a new generation of materials thanks to their superior optoelectronic properties and better stability than hybrid organic–inorganic perovskites. In particular, cesium lead bromide ($CsPbBr_3$) exhibits advantageous properties for numerous applicative fields (photovoltaics, light-emitting diodes, photodetectors, lasing, field effect transistors, and ionizing radiation detectors). The performance of $CsPbBr_3$ being critically dependent on the deposition technique, proper understanding and optimization of the fabrication process are demanding. Despite the well-known potentiality of the Pulsed Laser Deposition (PLD) technique in depositing films with complex stoichiometry, a very limited number of literature studies report on the successful deposition of $CsPbBr_3$ films by PLD. Recently, the authors disclosed the impact of the uneven masses of Cs, Pb, and Br on the film stoichiometry and guidelines to recover the desired composition. Herein, we exploit stoichiometric mechano-chemically synthesized targets to deposit, by nanosecond-PLD ($\lambda = 248$ nm, $\tau = 20$ ns, room temperature, fluence of 1 J/cm^2), $CsPbBr_3$ films to be studied following time aging, thermal heating and exposure to high relative humidity. Even in the presence of the characteristic absorption peak at ~ 520 nm, the freshly deposited film shows no photoluminescence. Photoluminescence is switched on by thermal annealing (at 250 and 350 °C) or after a few days (at least 15) of exposure to air and it persists over time. Films present interesting morphology evolution and oxygen adsorption following heating.

Keywords All-inorganic perovskite · $CePbBr_3$ · Laser ablation · Annealing effects

1 Introduction

The three-component all-inorganic lead halide perovskite $CsPbBr_3$ system has witnessed increasing interest from researchers around the global community following its first successful preparation in nano-crystalline form in 2015 [1]. This successful spreading of interest in applications relies on the low cost and superior photophysical properties of $CsPbBr_3$, including higher stability against high humidity and thermal environmental conditions compared with organic and hybrid perovskites, high chemical stability, high melting point (> 500 °C), large absorption coefficient, wide color gamut, high stability against photobleaching, robustness against humid environments, high photoluminescence quantum yields and narrow emission linewidths, photoluminescence emission tunable by changing the composition, high electron mobility and long electron life time, high defect tolerance, and low-threshold lasing [2–7]. Nowadays, all-inorganic $CsPbBr_3$ are exploited in numerous applicative fields [8–12], including photovoltaics [13–16], lasing [17], light-emitting diodes [18, 19], photodetectors [20], color-conversion layers [21], high-energy radiation detection [22], clinical radiotherapy [23], and scintillators [24].

✉ Anna Paola Caricato
annapaola.caricato@unisalento.it

1 Department of Mathematics and Physics "Ennio De Giorgi", University of Salento, 73100 Lecce, Italy

2 CEDAD (Centro of Applied Physics, Dating and Diagnostics), Department of Mathematics and Physics "Ennio De Giorgi, University of Salento-Lecce, Lecce, Italy

3 INFN (National Institute of Nuclear Physics), Lecce, Italy

4 Department of Biological and Environmental Sciences and Technologies (DiSTeBA), University of Salento, 73100 Lecce, Italy

5 Department of Innovation Engineering, University of Salento, 73100 Lecce, Italy

The ideal structure of $CsPbBr_3$ can be depicted as consisting of corner-sharing $[PbBr_6]^{-4}$ octahedral building blocks with the Cs^+ cation occupying the 12-fold coordination site in the middle of the cube of eight $[PbBr_6]^{-4}$ octahedrons. Lead halide perovskite exhibits a rich and complex phase diagram. It forms three distinct crystal lattices (orthorhombic, tetragonal, and rhombohedral phases with lower symmetry than the cubic ideal phase) depending on the tilting of the corner-sharing $[PbBr_6]^{-4}$ octahedral building blocks. Transformations between the existing polymorphs are temperature dependent. For instance, bulk $CsPbBr_3$ assumes a yellow orthorhombic phase at room temperature and the crystal phase symmetry can be driven by temperature: bulk $CsPbBr_3$ undergoes orthorhombic-to-tetragonal phase transition at ~ 88 °C and tetragonal-to-the orange cubic phase transformation at ~ 130 °C [25].

Moreover, depending upon the ratio of Cs/Pb, the formation of three ternary compositions can occur, namely $CsPbBr_3$ and the spurious Cs-rich Cs_4PbBr_6 and Br-rich $CsPb_2Br_5$ phases [19, 26, 27] according to the spontaneous reactions

$$CsBr + 2PbBr_2 \rightarrow CsPb_2Br_5$$

$$CsPbBr_3 + PbBr_2 \rightarrow CsPb_2Br_5$$

$$4CsBr + PbBr_2 \rightarrow Cs_4PbBr_6$$

$$3CsBr + CsPbBr_3 \rightarrow Cs_4PbBr_6.$$

Despite the useful "defect tolerance" of $CsPbBr_3$, shallow and deep defect states, oxidation, and external environmental conditions may affect remarkably the optoelectronic response not only of perovskite nanocrystals, due to the relevant role of the surface-to-volume ratio, but also of polycrystalline films and bulk samples. In practice, $CsPbBr_3$ may suffer from degradation of its photoluminescence caused by air exposure, moisture, illumination, heating, and loss of the halide atoms [28–31]. In this respect, several strategies were developed aiming at improving stability against external environmental conditions: encapsulation of halide perovskite nanocrystals in inert matrices, such as TiO_2 and crosslinked SiO_2 matrix [32–34] or in polymer materials [35, 36], halide perovskite nanocrystals coated with Al_2O_3 [37], and in-situ passivation of $CsPbBr_3$ by the air-stable Cs-rich Cs_4PbBr_6 phase [38] that works without additive impacting on the complexity of the preparation and photophysical properties of perovskites.

Main concerns regarding the performance of $CsPbBr_3$-based devices are the critical impact of both fabrication technique, such as in the case of wet (solution-based) methods and dry vacuum methods, and dimensionality, with films being more suitable and stable than nanocrystals for integrated optoelectronic applications [39].

Wet chemistry synthesis is carried out based on two different methods: the single-step approach mixes stoichiometric ratio of both precursor salts in a common solvent that is allowed to evaporate to obtain perovskite powders to be processed depending on the application; the two-step approach dissolves the precursors into different solvents, the obtained suspensions are deposited as thin films and then annealed to form the perovskite material. Although the experimental equipment needed for solution-assisted synthesis of $CsPbBr_3$ is cheap, criticisms related to the different solubility of the CsBr and $PbBr_2$ precursor salts in aprotic solvents are responsible of the precipitation of spurious phases alongside the desired $CsPbBr_3$ phase [19, 40, 41], hence leading to poor control on reproducibility, uniformity, and composition in particular over large area substrates. More generally, wet (solution-based) methods need hazardous chemicals and capping ligands, suffer from a restricted number of solvents and their inability to work in dissolving effectively all precursors cause solvent residuals, affect morphology and crystallization quality of the final product, and require multistep and time-consuming processing to produce gram-scale amounts of $CsPbBr_3$ powders to be further processed.

A solvent-free alternative to wet-chemistry synthesis of $CsPbBr_3$ powders is mechano-chemical synthesis, that exploits the reaction of halide salts triggered by mechanical energy [42, 43], and is particularly suited as a preliminary step to dry vacuum-assisted methods for growing films. A technique largely exploited for depositing thin films starting from compacted powder targets is pulsed laser deposition (PLD). It was recently discussed, in terms of stoichiometry transfer and impact of the mass distribution of Cs, Pb, and Br in the plasma plume, to growth good-quality luminescent $CsPbBr_3$ films using targets prepared by thermally assisted mechano-chemical synthesis [41]. A relevant finding of this preliminary study was that the simultaneous presence of heavy and light species in $CsPbBr_3$ implies films suffering from Pb-excess and Br-deficiency if a conventional 1:1 molar ratio target is prepared. It was demonstrated that properly annealed Cs-rich mechano-chemical targets make the PLD technique a successful vacuum-assisted approach to prepare luminescent $CsPbBr_3$ films.

To extend the knowledge of the potential of PLD in growing $CsPbBr_3$ films, in this paper, we explore the implications of a stoichiometric mixture of $PbBr_2$ and CsBr powders (molar ratio 1:1) to manufacture $CsPbBr_3$ compacted targets to be ablated by pulsed excimer laser. As the resulting PLD-deposited films suffer from Br-deficiency, due to the uneven mass of the involved elements and stoichiometric target, it may be interesting to investigate possible strategies to tune and enhance their photoluminescence performances on accounting for the unique ability of PLD to tune

composition, morphology, and thickness [41]. This aim is well motivated by several interesting and not fully understood or studied results regarding the controversial influence of the external environment conditions on the emission properties of perovskite materials.

For instance, chemisorption and/or physisorption of gaseous molecules at the air–perovskite surface was demonstrated to impact on the optical properties of hybrid halide perovskites [44–46] and $CsPbBr_3$ nanocrystals due to their sensitivity to surroundings favored by high surface/volume ratio [31, 47, 48]. On the other hand, oxygen passivation of the halide vacancies at the air–perovskite interface can act in improving the photoluminescence performances [47, 49, 50]. However, ambiguous results are reported about humidity, that may be beneficial or deleterious depending on the manufacturing process, micro- or nano-crystalline nature of the sample, aging/storing conditions, and protocol of exposure to the relative humidity [51].

In this paper, we investigate the PLD-growth of Br-deficient films and the impact on their emission properties of aging, post-growth thermal annealing at different temperatures, and exposure to relative humidity. Noteworthy, solvent-free preparation of the target and growth under high vacuum enables high surface quality of the PLD-grown films that are critical to minimize surface defect states stemming from ligands and contaminants. Hence, PLD-grown Br-deficient $CsPbBr_3$ films are ideal to study the interplay between Br-vacancies and post-growth processing involving different ambient conditions.

2 Experimental methods

2.1 Preparation of the $CsPbBr_3$ ablation targets

Solid pellets of compacted $CsPbBr_3$ powders were manufactured by the all-solid-state mechano-chemical synthesis approach [52] according to the following procedure.

The binary CsBr and $PbBr_2$ precursors (purchased by Chempur, 99.9% grade purity) were hand grinded and mixed, in equal molar ratio and without further purification, for 15–20 min [53, 54] at room temperature in air. The mixture was observed to change its color from white to yellow–orange, that was indicative of the formation of the $CsPbBr_3$ compound. Consistently, studies on the reaction kinetics of mechano-chemically synthesized $CsPbBr_3$ powders handled at room temperature by mixing the precursor salts in stoichiometric quantity report complete reaction occurring in less than 10 min [43]. Since we mixed 1:1 molar ratio $PbBr_2$: CsBr, corresponding to a stoichiometric mixture, the reaction $3PbBr_2 + Cs_4PbBr_6 \rightarrow 4CsPbBr_3$ may not work advantageously to remove the spurious phase in the absence of $PbBr_2$ in excess [41]. Alternatively, as the transformation of the Cs_4PbBr_6 phase to $CsPbBr_3$ can be driven thermally, thermal annealing of the mixed reacted powder was exploited to yield the desired phase.

Therefore, the obtained powder was compacted by means of the application of the 6-ton pressure through a hydraulic press. The resulting compressed solid pellet was transferred to an oven where it was thermally annealed in two steps: first step, heating at 400 °C for 2 h and, second step, further heating at 500 °C for 2 h. Finally, the oven was switched off and the target was let cool down to room temperature before being kept in a plastic box within a vacuum ball and under darkness until their usage in PLD depositions. A comprehensive discussion of the interplay between composition of the $PbBr_2$–CsBr mixture and thermal annealing protocol in preparing the compacted targets was reported elsewhere [41].

2.2 Pulsed laser deposition experiments

PLD experiments were performed by exploiting the excimer laser set-up depicted in Fig. 1a that consists of a pulsed excimer KrF laser (Lambda Physics, operating wavelength 248 nm, and pulse width $\tau_p = 20$ ns), quartz optics to focus the laser beam, a stainless-steel vacuum chamber, a target and a substrate holder rotating independently, and rotative and turbo pumps. Once the ablation mechanism onsets, a forwardly peaked plasma plume forms including the species ejected from the target that, while expanding in vacuum, are transferred from the target to the substrate where the growth of the deposit occurs driven by the hyperthermal kinetics and super-saturated deposition flux peculiar of PLD [55].

In our experiments, the excimer laser beam was incident at 45° with respect to the surface of the mechano-chemically synthesized $CsPbBr_3$ targets, mounted on a rotating target holder (frequency of 3 Hz) and kept at room temperature. The pulsed laser beam was focused with a fluence (i.e., energy delivered per pulse and per unit surface) $F = 1$ J/cm^2 at the frequency of 5 Hz. PLD depositions were performed under high-vacuum conditions (background pressure as low as $\sim 10^{-5}$ Pa) after cleaning the target surface by 1000 laser pulses fired at 10 Hz while screening the substrate by a shutter to avoid its contamination.

The silica substrate, cleaned in acetone and ethanol for 10 min at 60 °C each, was placed at the distance of $d_{T-S} = 4$ cm from the target with substrate axis shifted by ~ 4 mm with respect to the plume axis. Moreover, the substrate was rotated, with a rotation frequency of 1.2 Hz, while growing the film to improve film uniformity [56]. A number of 1000 and 2000 laser pulses were fired to deposit the films of interest in this study.

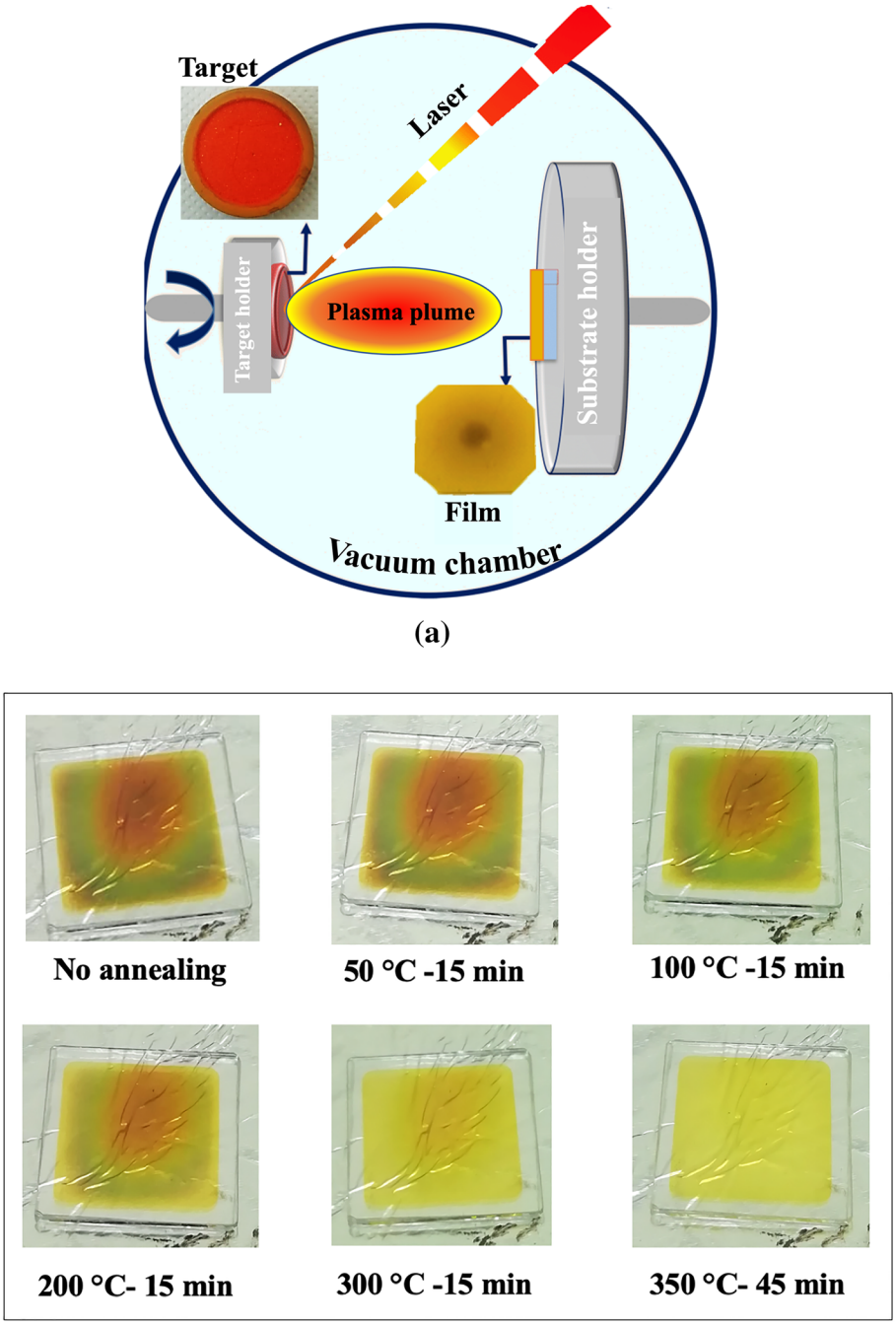

Fig. 1 **a** Schematic diagram of a PLD experiment; **b** visual evolution of a PLD-deposited $CsPbBr_3$ film ($F = 1$ J/cm^2, 1000 pulses) subjected to thermal annealing up to 350 °C

2.3 Post-growth treatments

Films deposited according to the above-detailed experiments were subjected to time aging under controlled conditions (storing in a plastic box at 10^{-2} Pa to minimize air exposure, under dark) to gain knowledge about eventual changes in the emission properties.

Moreover, freshly deposited samples were subjected to post-growth thermal treatments according to two different protocols: heating up to 250 °C allowing temperature to increase of 50 °C at each step (50 °C for 15 min, 100 °C for 15 min, 150 °C for 15 min, 200 °C for 60 min, and 250 °C for 60 min) and heating up to 350 °C with temperature increasing of 50° or 100 °C at each step (50 °C for 15 min, 100 °C for 15 min, 200 °C for 15 min, 300 °C for 15 min, and 350 °C for 45 min), Fig. 1b.

The impact of the combined exposure to relative humidity (RH) and heating was studied by carrying out the annealing

protocol up to 250 °C under high RH conditions, that is RH = 60, 80%.

On the basis of the detailed experiments, the $CsPbBr_3$ films under discussion will be hereafter termed $CsPbBr_3$ (T, Np, RH), where T = RT, 250 °C, 350 °C stands for room temperature (RT) and the post-growth set annealing temperatures (i.e., 250 °C and 350 °C), Np = 1000, 2000 is the number of deposition laser pulses and RH refers to the relative humidity values set in our experiments (RH = 60–80%).

2.4 Characterization analyses

2.4.1 X-ray diffraction (XRD) analysis

To identify the crystal structure of the $CsPbBr_3$ films under consideration in this study, X-ray diffraction (XRD) spectra (Rigatu Company, Tokio, Japan) were acquired using a Cu Kα X-ray source of wavelength 1.54056 Å. The instrument worked at the voltage of 40 kV and operating current of 40 mA. The X-ray pattern of the specimen of interest was acquired over the angular range $2\theta = 10–50°$.

2.4.2 Rutherford backscattering (RBS) analysis

Rutherford backscattering spectrometry (RBS) was implemented to determine the stoichiometry and thickness of the deposited $CsPbBr_3$ films. RBS measurements were carried out at the in-vacuum IBA beamline at CEDAD (Centre of Applied Physics, Dating and Diagnostics), University of Salento [57]. The samples were irradiated with 2.0 MeV He^{2+} particles. Backscattered particles were detected at an angle of 170° using a PIPS (Passivated Implanted Planar Silicon), detector by Canberra, Montigny-Le-Bretonneux, France Idem [58]. Data acquisition was carried out using the Canberra Genie Software (GENIE™ 2000, Basic Spectroscopy Software by Canberra Industries, Meriden, CT, USA) and experimental data were fitted by the SIMNRA code (version 7.0, Matej Mayer, Max Plank Institute for Plasma Physics, Garching, Germany) [58].

2.4.3 Atomic Force Microscopy (AFM) analysis

The Atomic Force Microscopy (AFM) technique was exploited to image topography maps. A Park XE-70 Instruments microscope (Park Systems, Suwon, Korea) was used, operating under non-contact mode at room temperature and in air environment. The imaging scan size was set at 10×10 μm^2. Average roughness Ra was estimated to characterize the roughness of the PLD-deposited films and was evaluated as arithmetic average over 5 measures.

2.4.4 XPS

XPS analysis were performed with an AXIS ULTRA DLD (Kratos Analytical) spectrometer equipped with an Al Kα (1486.6 eV) monochromatic source (line width 0.2 eV), operating at 10 kV and 15 mA (150 W). Survey spectra were collected at pass energy of 160 eV and step size of 1 eV over the energy range of 0–1400 eV. High-resolution (HR) spectra acquisition (C1s, O1s, Br 3d, Pb4f, and Cs3d) was recorded at a pass energy of 20 eV. The measured pressure in the analysis chamber was in average 1.0×10^{-9} torr during the acquisitions.

The XPS spectra were collected on films deposited on silica slides (2 cm × 2 cm) and opportunely fixed on the sample stab. A hybrid lens mode was used for all measurements with analysis area of about 700 µm × 300 µm. During the data acquisition, a careful charging effect correction has been made using the charge neutralization with a filament current, filament bias voltage, and charge balance voltage of 2.0 A, 1.3 V, and 3.6 V. Data analysis of high-resolution spectra was performed using the fitting program CASA-XPS. All the experimental BE values were correct by setting the binding energy of C1s hydrocarbon photo-peak at 285.0 eV used as an internal standard [59]. Peaks assignment has been done by comparing the binding energy to that reported in the literature and in the standard reference database of the National Institute of Standard and Technology (NIST X-ray Photoelectron Spectroscopy Database). Peak areas were converted to atomic percent (At%) using established procedures and the appropriate sensitivity factors (SF) to ensure the correct elemental mass balance, [62]. All obtained, binding energy and atomic compositions were representative of the mean values obtained on minimum three different spots of the analyzed samples. XPS elemental composition allowed to identify and to quantify the elements present in the analyzed samples.

2.4.5 Absorbance and PL measurements

The optical properties of the $CsPbBr_3$ films were studied by UV–Vis absorbance and photoluminescence (PL). Absorbance spectra were measured by a PerkinElmer Lambda 900 UV spectrophotometer (PerkinElmer Company, Waltham, MA) over the wavelength range from 200 to 800 nm and with a wavelength resolution of 3 nm.

Photoluminescence curves were acquired by a solid-state continuous-wave (CW) laser delivering 100 mW at 405 nm with a diameter spot of 2 mm. The emission signal was collected in backscattering configuration by an optical fiber connected to a compact CCD (Oceanoptics) delivering a PL signal to the whole UV–Vis–NIR spectral window.

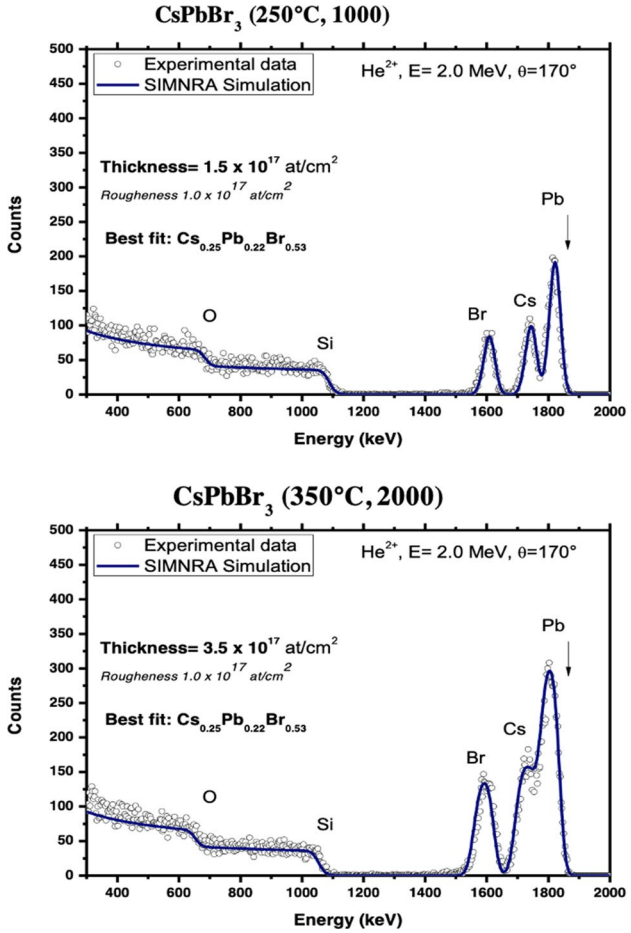

Fig. 2 RBS-based compositional and thickness characterization of $CsPbBr_3$ (250 °C, 1000) (top-most panel) and $CsPbBr_3$ (350 °C, 2000) (bottom panel)

3 Results and discussion

3.1 Compositional, structural, and morphological characterization

The composition of the films under study was estimated by the RBS technique. As a result of RBS fitting of the measured spectra, the Br-deficient composition $Cs_{0.25}Pb_{0.22}Br_{0.53}$ was calculated for the as-deposited $CsPbBr_3$ (RT, 1000) film**.** Increased number of laser pulses (2000) and thermal treatment were found to induce no detectable change in the film stoichiometry. Indeed, as Fig. 2 shows, the same composition as $CsPbBr_3$ (RT, 1000) was estimated for both $CsPbBr_3$ (250 °C, 1000) and $CsPbBr_3$ (350 °C, 2000). It is worth observing that, in general, annealing is implemented to improve grain morphology and size as well as crystallinity of polycrystalline $CsPbBr_3$ films [61]. As mass loss of $CsPbBr_3$ starts at a temperature higher than 350 °C [62], the above result confirms the expected absence of impact of the set maximum annealing temperature on the composition of the annealed films. Since it was not possible to determine the oxygen presence by RBS analyses because of the substrate composition, XPS analysis was performed, as detailed hereafter.

RBS analysis was also exploited to calculate film thickness: on turning from 1000 to 2000 laser pulses, the film was found to thicken from 1.5×10^{17} at/cm^2 to 3.5×10^{17} at/cm^2. Noteworthy, as detailed in the experimental, the substrate axis was shifted by ~ 4 mm with respect to the plume axis and rotated while growing the film to improve film uniformity [41]. As a result, a thickness difference of nearly 7% was measured on going from the center to the size of the film that is responsible of the different appearance of the as-grown film shown in Fig. 1b. The annealing temperature being lower than the evaporation temperature of $CsPbBr_3$, the observed change in the appearance of the film for increasing duration of the thermal annealing can be ascribed to improved structural order (as it will be discussed hereafter).

X-ray diffraction pattern (XRD) presented in Fig. 3 shows the co-existence of the thermodynamically stable phase at room temperature, i.e., orthorhombic $CsPbBr_3$ (pdf card #18-0364), and the Cs-rich Cs_4PbBr_6 phase (pdf card #73-2478) [41]. This issue is not surprising, because the $CsPbBr_3$ and Cs_4PbBr_6 phases tend to coexist [63, 64], Cs_4PbBr_6 has formation energy lower than the Br-rich Cs_2PbBr_5 ternary compound [43] and the films under study have Br-deficient composition. This implies that the reaction $3PbBr_2+Cs_4PbBr_6\rightarrow4CsPbBr_3$ is not likely to work to induce consumption of the spurious phase due to the absence of $PbBr_2$ in excess. Noteworthy, non-uniform distributions of residual Cs^+ and Br^- are improbable to play a role in

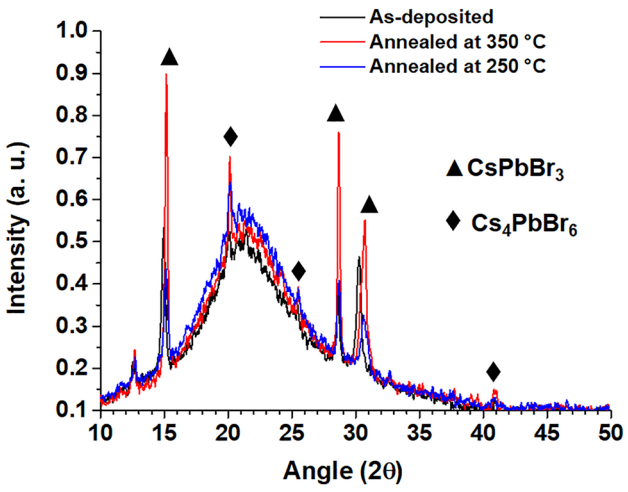

Fig. 3 XRD spectra of the as-deposited $CsPbBr_3$ film (continuous gray line), $CsPbBr_3$ (250 °C, 1000) (continuous blue line), and $CsPbBr_3$ (350 °C, 2000) (continuous red line)

accounting for the presence of Cs_4PbBr_6, because the Br-rich phase does not form at all.

Regarding the XRD spectrum of $CsPbBr_3$ (RT, 1000) shown in Fig. 3, the relatively broad diffraction lines and the relevant background contribution suggest that the sample consists of small crystallites within a nearly amorphous phase that is expected in the case of PLD-assisted growth at room temperature and under low fluence conditions. For comparison with the literature card, the diffraction peaks at 15.2°, 21.6°, and 30.6° are assigned to the (100), (110), and (200) orientation of $CsPbBr_3$ lattice planes, respectively. The occurrence of preferential crystalline orientations, even under room temperature growth conditions, can be ascribed to the PLD-related effective hyperthermal growth kinetics. Even if further diffraction features are hidden in the background, the intensity and width of the dominant diffraction lines at $2\theta = 15°$, 30° indicate dominance of the $CsPbBr_3$ with respect to the Cs-rich phase.

Figure 3 also shows the changes induced by the performed thermal treatments on the XRD diffractogram. Coexistence of the $CsPbBr_3$ and Cs-rich phases is retained in any case, that is not surprising given the above detailed Br-deficiency of the films.

In particular, it can be observed that the annealing treatment does not influence the peak position of the Cs-rich phase but eventually induces a slight increase in peak intensity above all for annealing temperature of 350 °C. On the other hand, the annealing treatment induces a shift toward larger angles of the main diffraction features. The annealing at 250 °C induced a shift from 15° to 15,2° and from 30.3° to 30.7° indicating the transition from the orthorhombic to cubic phase [61]. A further increase in the annealing temperature and number of laser pulses (see $CsPbBr_3$ (350 °C, 2000) vs $CsPbBr_3$ (250 °C, 1000) sample for comparison) induces an increase in peak intensity as well as reduction in their FWHM. This issue is indicative of increasing size of the characteristic length scale according to the Scherrer formula. Hence, refinement of the crystallinity alongside specific crystalline orientations clearly results under thermal treatment. As expected, the better structural refinement results from the interplay between annealing and increased number of laser pulses.

The same transformation was observed for as-deposited films after a few days (at least 15) of exposure to air.

Structural information resulting from XRD analysis suggests that compositional and morphological changes may occur because of aging and thermal annealing. Indeed, perovskite lattice presenting relatively weak lead–halogen bonds, environmental conditions may be responsible of structural and/or compositional changes. On the other hand, substantial evolution of grains and film morphology has been observed following thermal annealing [61] and exposure to humidity [51].

As shift of XRD peaks may be induced not only by structural and morphological modifications but also by chemical reactions (for instance, oxidation under air exposure), the occurrence of spurious surface bonding states was investigated by XPS analysis. Figure 4 enables to compare the XPS survey spectra of the as-deposited $CsPbBr_3$ film (continuous blue line) and the annealed $CsPbBr_3$ (350 °C, 1000) film (continuous yellow line). The high-resolution XPS spectra report Cs $3d_{5/2}$ peak signal at (724.5 ± 0.2) eV, Pb $4f_{7/2}$ at (138.4 ± 0.2) eV, Br $3d_{5/2}$ at (68.3 ± 0.2) eV, and the O_{1s} at (532.5 ± 0.2) eV. These values are in line with previous XPS data reported for $CsPbBr_3$-based perovskite [65]. As a result of the fitting, the surface calculated atomic ratio of each element is $Cs_{2.1}\,Pb_1Br_{2.6}$ for the as-deposited film and $Cs_{2.4}Pb_1Br_{2.6}O_{0.72}$ for the post-growth annealed film. From these data, it is evident a deficit of Br amount in both films surfaces as far as an enrichment in Cs, to respect Pb content. In addition, while no detectable signal belonging to not carbonaceous oxygen is observed in the as-deposited reference films, adsorbed molecular oxygen was detected in the case of the annealed films near to a well-resolved O1s

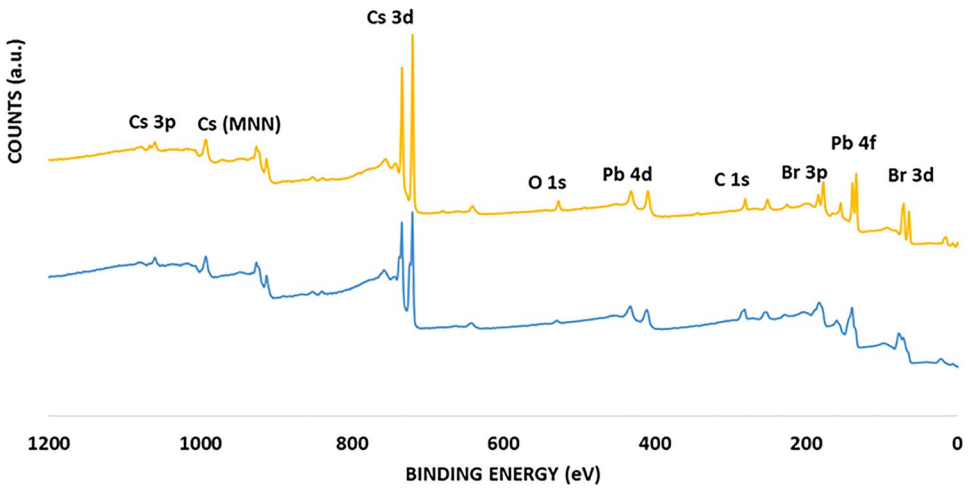

Fig. 4 XPS survey spectra on the as-deposited film (blue line) and the post-growth annealed film (orange line)

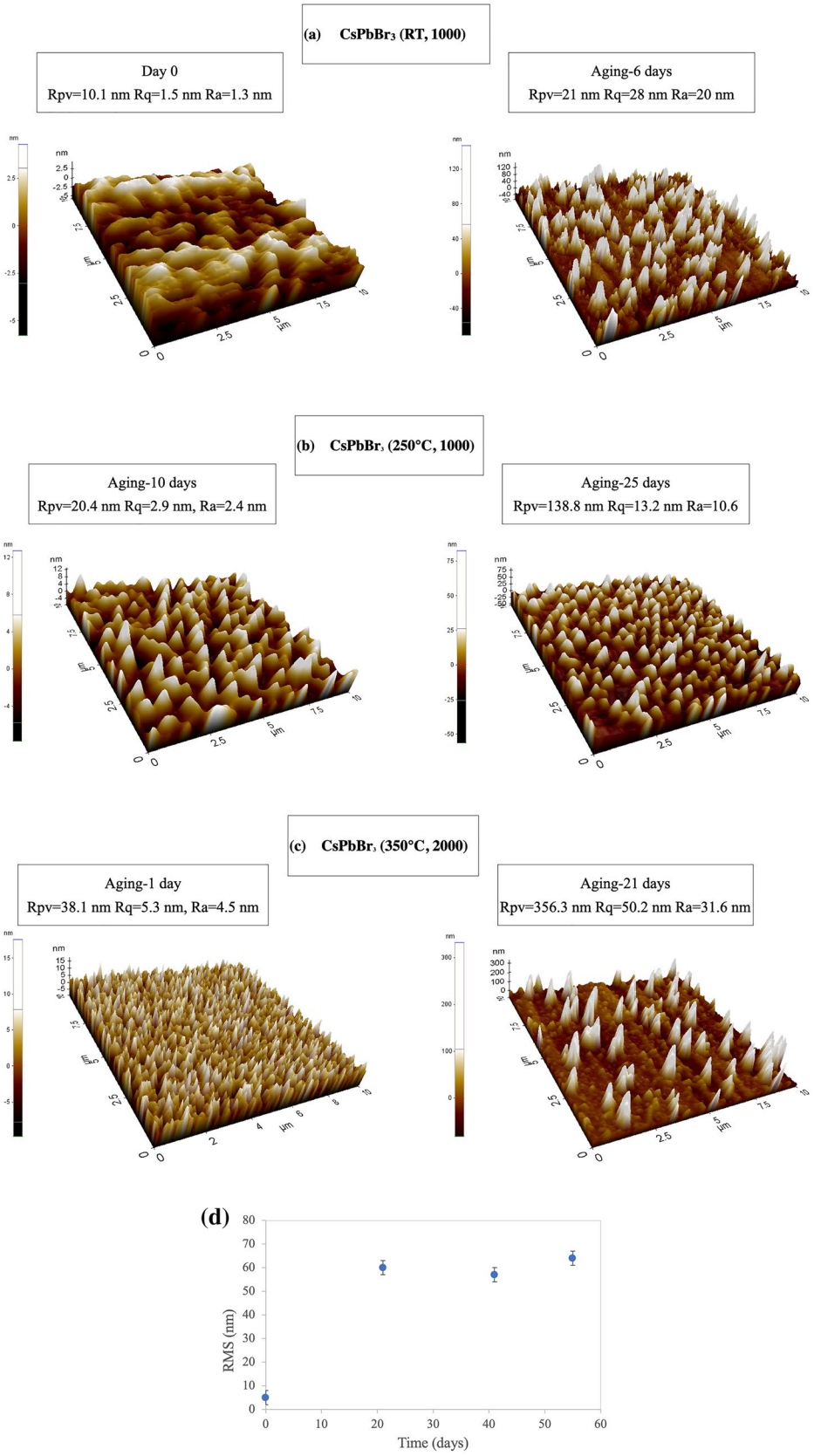

Fig. 5 AFM images of the **a** as-deposited sample soon after the deposition (left panel) and after 6-aging days (right panel); **b** thermal treated film at 250 °C after 10-aging days (left panel) and after 25-aging days (right panel); **c** thermal treated films at 350 °C after 1-aging day (left panel) and after 21-aging days (right panel); **d** root-mean-square roughness evolution of the thermal treated films at 350 °C

component observed at 529.3 ± 0.2, tentatively attributed to Pb–O bonds according to literature [66, 67]. Further studies are in progress to better investigate the chemical–physical state of oxygen present on the annealed surface film.

To correlate the structural information from XRD to heating-induced morphological changes, we measured AFM topography maps of the freshly deposited $CsPbBr_3$ (RT, 1000) film (Fig. 5a) aged for 2 and 6 days, $CsPbBr_3$ (250 °C, 1000) aged for 10 and 25 days following thermal annealing (Fig. 5b), and $CsPbBr_3$ (350 °C, 2000) (Fig. 5c) aged for 1 and 21 days following thermal annealing. It is interesting that the topographical properties of the annealed films change with time at room temperature and finally tend to stabilize after about 20 days (Fig. 5d).

Notably, $CsPbBr_3$ (RT) was found to undergo morphological evolution following its deposition, that is coalescence and transition from rounded to columnar-like shape of grains was observed over time (Fig. 5a). Consistently with the morphological changes, XRD analysis of $CsPbBr_3$ (RT) stored for 6 days (not reported herein) pointed out an intensity enhancement, sharpening, and slight shift to larger angles of the preferential orientations around 15° and 30°.

Very interestingly, the comparison between freshly prepared $CsPbBr_3$ (RT, 1000) (Fig. 5a) and $CsPbBr_3$ (250 °C, 1000) aged for 10 days (Fig. 5b, left panel) and 25 days (Fig. 5b, right panel) evidences a substantial morphological evolution. The film morphology changes from consisting of large and poorly defined grains concurring to a low-roughness film (Fig. 5a) to the occurrence of a distribution of clustered in-homogeneously arranged and dispersed micrometer-sized grains for aging lasting 10 days (Fig. 5b, left panel) and to densely packed columnar micrometric grains for aging further prolonged up to 25 days (Fig. 5b, right panel).

The morphological changes shown by AFM topography images are indicative of a growth/evolution mechanism by which the relatively void regions in between smaller grains are filled by a grain growth favoring their redistribution according to a more ordered coverage together with a columnar growth by Ostwald ripening. Consistently, average roughness changes from 2.9 nm to 13.2 nm and the peak-to-valley roughness increases from 20.4 nm to 138.8 nm for aging time prolonged from 10 to 21 days.

In the case of $CsPbBr_3$ (350 °C, 2000), the nucleation of a higher density of small grains is expected on the basis of the number of laser pulses increased from 1000 to 2000 that, as a consequence of a thicker deposit, may promote early morphological evolution toward the columnar-like grain morphology. This observation accounts for the morphology of $CsPbBr_3$ (350 °C, 2000) aged for 10 days (Fig. 5c, left panel) that, compared to the counterpart $CsPbBr_3$ (250 °C, 1000) (Fig. 5b, left panel), exhibits more densely packed and less size-dispersed grains. For aging prolonged from 1 to 21 days (Fig. 5c, right panel), $CsPbBr_3$ (350 °C, 2000) presents a relevant morphological change clearly indicative of the occurrence of Ostwald ripening: the sample exhibits a twofold distribution consisting of background sub-micron grains, residual of the early high-density finely grained distribution, and micrometer larger columnar grains formed by coalescence and growth at the expense of small grains. Average roughness increases from 4.5 nm to 31.6 nm and the peak-to-valley roughness jumps from 38.1 to 356.3 nm for aging time prolonged from 1 to 21 days. Under the experimental conditions under consideration, no further evolution was observed after 21 days.

The above detailed morphological evolution agrees with the XRD analysis: structural refinement better for $CsPbBr_3$ (350 °C, 2000) than for $CsPbBr_3$ (250 °C, 1000) and peak sharpening can be related to the occurrence of large columnar grains resulting from grain growth and coalescence driven by the interplay between high-temperature annealing and number of laser pulses.

It is worth reporting that no variation of the composition was exhibited by the samples under aging, that points out the evolution morphological as related to structural rearrangement of the samples to gain the thermodynamically steady-state structure following thermal annealing. Our experimental findings indicate that $CsPbBr_3$ evolves toward a columnar grain morphology [41].

Therefore, the reported time morphological evolution yielding to formation and/or refinement of the $CsPbBr_3$ phase reflects the transition to the most energetically favorable phase among the ternary allowed ones in films including residuals of a spurious phase and Br-deficiency.

3.2 Spectral characterization

Since the transition to a homogeneous grain structure with columnar orientations and without large hillocks can improve the photoluminescence performance of $CsPbBr_3$ films [68], we characterized the emission properties of our samples to relate them to the above compositional and morphological results.

Despite the dominant occurrence of $CsPbBr_3$, no photoluminescence emission was detected from the freshly deposited $CsPbBr_3$ (RT, 1000) film that, however, switched from no emission to weak green emission over the time. On accounting for the spontaneous morphological evolution of $CsPbBr_3$ (RT, 1000) under aging, its emission behavior can be related to structural reorganization effects. This relationship can be effectively studied by monitoring time aging of the annealed samples, which demonstrated remarkable morphological evolution.

Figure 6a reports the wavelength-dependent absorbance spectrum of $CsPbBr_3$ (RT), $CsPbBr_3$ (250 °C, 1000), and $CsPbBr_3$ (350 °C, 2000) in the visible range. Spectra

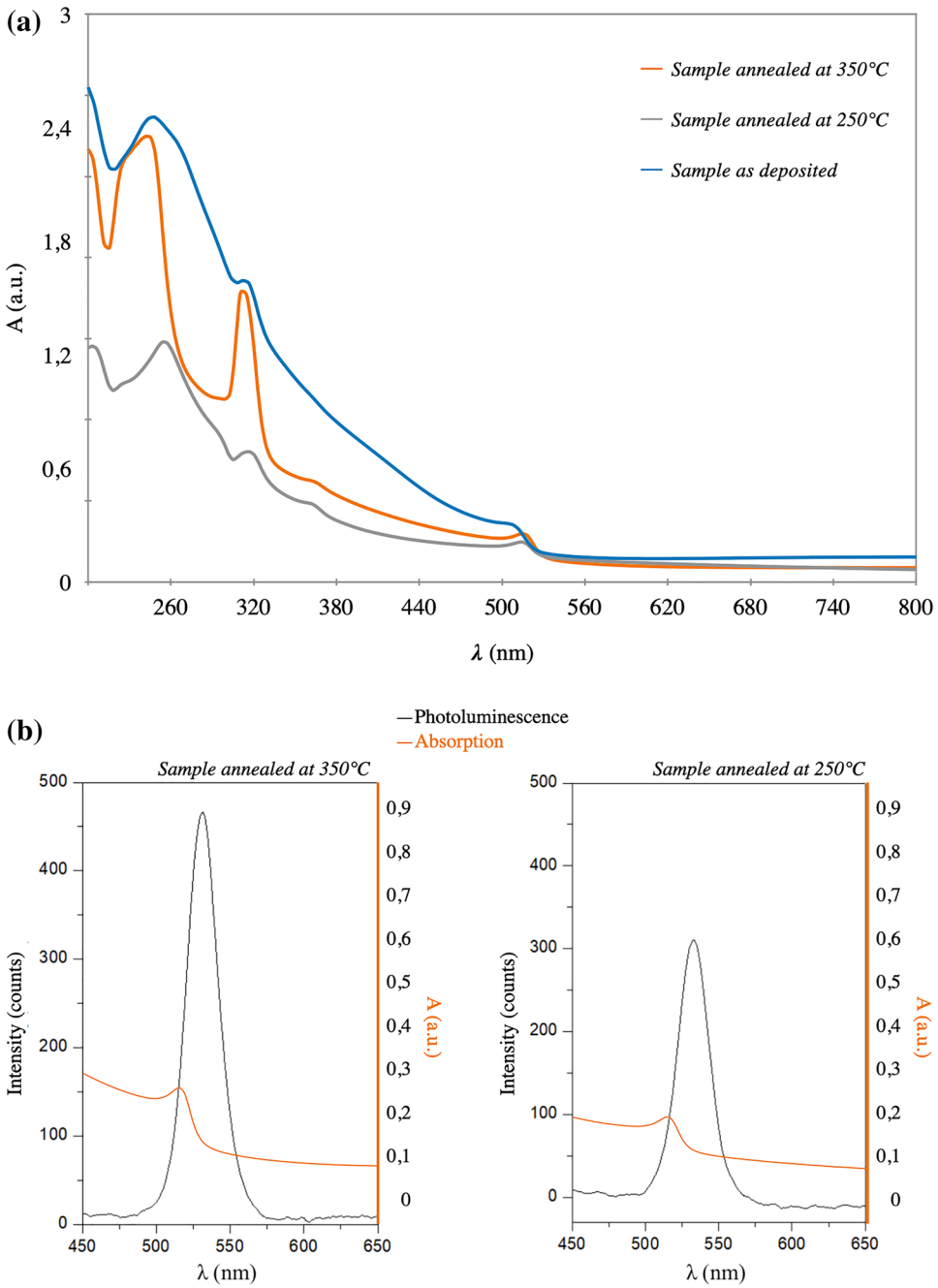

Fig. 6 **a** Absorption spectra of the Br-deficient as-deposited film (blue line); thermal annealed film in air at 250 °C (gray line); thermal annealed film in air at 350 °C (orange line); **b** PL and absorption spectra of the thermal annealed films in air at 250 °C (left panel) and at 350 °C (right panel)

exhibit common general features, such as a sharp onset around 530 nm and an excitonic peak at nearly 515 nm, while being affected by the thermal treatment. In the case of the reference sample, $CsPbBr_3$ (RT), the absorption feature at 516 nm matches the typical absorption edge of $CsPbBr_3$ corresponding to the excitonic recombination close to the edges of the direct band gap [19, 51, 61, 69]. Consistently with XRD analysis, a weak feature at 310 nm was also detected that can be attributed to the Cs_4PbBr_6 phase with bulk absorption in the range 305–330 nm [40, 63, 70]. The same spectral structure can be observed for the annealed samples with a temperature-dependent shift of the excitonic peak and increasing of the absorbance step for $CsPbBr_3$ (350 °C, 2000), in accordance with the crystal refinement indicated by XRD analysis. On comparing $CsPbBr_3$(250 °C, 1000) and $CsPbBr_3$ (350 °C, 2000), the larger absorbance intensity is consistent with $CsPbBr_3$ (350 °C, 2000) being the thickest film.

The Tauc plot method was implemented to estimate the energy band gap that was found to be (2.3 ± 0.1) eV for

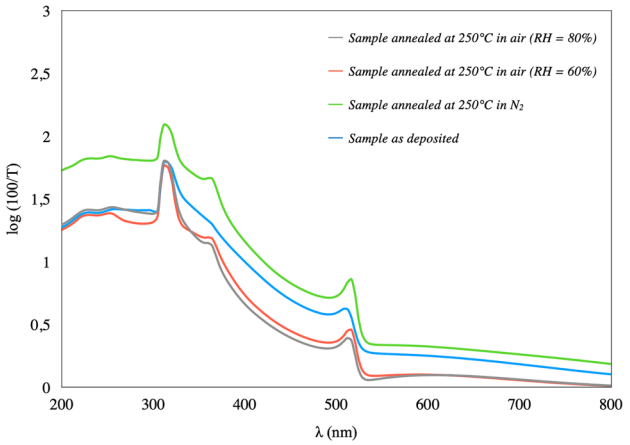

Fig. 7 Absorption spectra of the films under study: Br-deficient as-deposited film (blue line); thermal annealed film in air at 250 °C RH = 60% (red line); thermal annealed film in air at 250 °C RH = 80% (gray line); thermal annealed film in N_2 at 250 °C RH = 60% (green line)

both $CsPbBr_3$ (250 °C, 1000) and $CsPbBr_3$ (350 °C, 2000) films, in accordance with the literature [61, 69, 71].

Figure 6b shows the PL spectra of $CsPbBr_3$ (250 °C, 1000) and $CsPbBr_3$ (350 °C, 2000) films together with the associated absorption curve. The PL curves are characterized by a wide and intense emission band spectrally located in the green region.

The PL peak is located at 532 nm for both $CsPbBr_3$ (250 °C, 1000) and $CsPbBr_3$ (350 °C, 2000) films, while an FWHM of ~ 25.7 nm was reported for $CsPbBr_3$ (250 °C, 1000) and $CsPbBr_3$ (350 °C, 2000), respectively.

To assess the role of thermal annealing in inducing PL, we carried out transmission measurements of perovskite films annealed at 250 °C in air with a different value of relative humidity (RH = 60%, 80%) and in N_2 compared to the as-deposited sample. All the spectra show the typical sharp onset of $CsPbBr_3$ at nearly 530 nm and the characteristics features of the $CsPbBr_3$ and Cs_4PbBr_6 phases (Fig. 7). It is clear that, as well as for the light emission properties, the annealing treatment improves the transmission of the films if they are exposed to humid air but not to other gases such as N_2. A proper exposure to humidity (RH = 60% for 48 h or RH = 80% for 8 min) may indeed improve the crystalline quality of $CsPbBr_3$ even at room temperature due to the increase in the mobility of ionic species, although prolonged exposure under uncalibrated RH conditions causes the degradation of $CsPbBr_3$ into its spurious phases ($CsPb_2Br_5$ and/or Cs_4PbBr_6) [51]. Moreover, high humidity was found to remarkably enhance the grain size and induce a reduction of the step height of the absorbance spectrum due to degradation of the surface of $CsPbBr_3$ films [72]. Our experimental finding indicates that the as-deposited $CsPbBr_3$ phase film suffers from the presence of trap states that negatively impact on their PL yield, but it can show post-growth grain morphology evolution leading to light emission over long time. On the contrary, heating under humid air facilitates oxygen adsorption that partially passivates the halide vacancies [47, 49, 50]. Noteworthy, the films annealed in air as well as the as-deposited one (once the PL has been activated) retain their emission properties for long time (1 year at least).

4 Conclusions

In this study, we have presented Br-deficient $CsPbBr_3$ films deposited by laser ablation of stoichiometric mechanochemically synthesized targets. The films are polycrystalline with both Cs_4PbBr_6 and $CsPbBr_3$ phases, the $CsPbBr_3$ orthorhombic phase being the dominant contribution. Time aging or thermal annealing protocols (at 250 °C for 60 min and 350 °C for 45 min) are such to promote the crystal refinement of the $CsPbBr_3$ phase that has been discussed by the temperature-dependent changes in the XRD spectra. In any case, the morphology of the films has been shown to undergo grain evolution after the deposition that tends to stabilize after 20 days in the case of the films annealed in air. Noteworthy, a characteristic surface topography consisting of micrometer-sized columnar-like grains has been reported for the annealed films over time aging.

Elemental analysis has demonstrated that the composition is retained under annealing in air, apart from oxygen adsorption that has been demonstrated to be beneficial in terms of PL performances.

Soon after the deposition, the films do not present detectable PL as related to a high density of trap states and absence of morphological stabilization. Indeed, even the as-deposited sample emits once stored and the gained PL properties occur together with morphological evolution.

Thermal treatments in presence of RH favor ion mobilities, impacting on grain growth, and accelerate the oxygen adsorption by Br-vacancy-related intra-gap trap states. As a result, switching on of the PL onsets and emission persists over time. The same effect of improved and long-lasting PL yield has been shown to occur following prolonged exposure to high levels of RH. In this respect, our findings are very interesting, because at the high RH set in our experiments, a degradation of the PL performances would have been expected based on the literature.

Definitively, we have reported PLD as a promising fabrication technique in that it allows the deposition of $CsPbBr_3$ films stable over long times even when exposed to high relative humidity conditions. More insight in this relevant issue would require a careful investigation of the ablation mechanisms as impacted by the key deposition

parameters, such as fluence, repetition rate, number of laser shots, and pulse duration. Moreover, further experiments could allow deep understanding of the role of and interplay between thermal annealing, occurrence of Br-vacancies and their saturation by oxygen under exposure to humidity over time.

Questions arisen in this study will be the subject of a future study.

Funding Open access funding provided by Università del Salento within the CRUI-CARE Agreement.

Declarations

Conflict of interest There are no conflicts to declare.

References

1. L. Protesescu, S. Yakunin, M.I. Bodnarchuk, F. Krieg, R. Caputo, C.H. Hendon, R.X. Yang, A. Walsh, M.V. Kovalenko, Nano Lett. (2015). https://doi.org/10.1021/nl5048779
2. Y. Zhou, Y. Zhao, Energy Environ. Sci. (2019). https://doi.org/10.1039/C8EE03559H
3. H. Chen, S. Xiang, W. Li, H. Liu, L. Zhu, S. Yang, Sol. RRL (2018). https://doi.org/10.1002/solr.201700188
4. M.V. Kovalenko, L. Protesescu, M.I. Bodnarchuk, Science (2017). https://doi.org/10.1126/science.aam7093
5. Y. Chen, E. Orgiu, ChemNanoMat (2019). https://doi.org/10.1002/cnma.201800679
6. S. Seth, N. Mondal, S. Patra, A. Samanta, J. Phys. Chem. Lett. (2016). https://doi.org/10.1021/acs.jpclett.5b02639
7. Y. Kanemitsu, T. Handa, Jpn. J. Appl. Phys. (2018). https://doi.org/10.7567/JJAP.57.090101
8. N.G. Park, Mat. Today (2015). https://doi.org/10.1016/j.mattod.2014.07.007
9. Q.A. Akkerman, M. Gandini, F. Di Stasio, P. Rastogi, F. Palazon, G. Bertoni, J.M. Ball, M. Prato, A. Petrozza, L. Manna, Nat. Energy (2016). https://doi.org/10.1038/nenergy.2016.194
10. K. Lin, J. Xing, L.N. Quan, F.P.G. de Arquer, X. Gong, J. Lu, L. Xie, W. Zhao, D. Zhang, C. Yan, W. Li, X. Liu, Y. Lu, J. Kirman, E.H. Sargent, Q. Xiong, Z. Wei, Nature (2018). https://doi.org/10.1038/s41586-018-0575-3
11. G. Raino, M.A. Becker, M.I. Bodnarchuk, R.F. Mahrt, M.V. Kovalenko, T. Stoferle, Nature (2018). https://doi.org/10.1038/s41586-018-0683-0
12. M. Liu, M.B. Johnston, H.J. Snaith, Nature **501**, 395 (2013)
13. S. Ullah, J. Wang, P. Yang, L. Liu, S. Yang, T. Xia, H. Guo, Y. Chen, Mater. Adv. (2020). https://doi.org/10.1039/D0MA00866D
14. C. Vidyasagar, B.M.M. Flores, V.M.J. Pérez, Nano-Micro Lett. (2018). https://doi.org/10.1007/s40820-018-0221-5
15. G. Tong, L.K. Ono, Y. Qi, Energy Technol. (2020). https://doi.org/10.1002/ente.201900961
16. N. Kumar, J. Rani, R. Kurchania, Sol. Energy (2021). https://doi.org/10.1016/j.solener.2021.04.042
17. S. Yakunin, L. Protesescu, F. Krieg, M.I. Bodnarchuk, G. Nedelcu, M. Humer, G. De Luca, M. Fiebig, W. Heiss, M.V. Kovalenko, Nat. Commun. (2015). https://doi.org/10.1038/ncomms9056
18. J. Song, J. Li, X. Li, L. Xu, Y. Dong, H. Zeng, Adv. Mater. (2015). https://doi.org/10.1002/adma.201502567
19. N. Yantara, S. Bhaumik, F. Yan, D. Sabba, H.A. Dewi, N. Mathews, P.P. Boix, H.V. Demir, S. Mhaisalkar, J. Phys. Chem. Lett. **5**, 5 (2015). https://doi.org/10.1021/acs.jpclett.5b02011
20. P. Ramasamy, D.-H. Lim, B. Kim, S.-H. Lee, M.-S. Lee, J.S. Lee, Chem. Commun. (2016). https://doi.org/10.1039/C5CC08643D
21. Y. Yin, M.U. Ali, M. Liu, J. Miao, W. Peng, D. Li, S. Chen, C. Lee, H. Meng, Small (2019). https://doi.org/10.1002/smll.201901954
22. C.C. Stoumpos, C.D. Malliakas, J.A. Peters, Z. Liu, M. Sebastian, J. Im, T.C. Chasapis, A.C. Wibowo, D.Y. Chung, A.J. Freeman, B.W. Wessels, M.G. Kanatzidis, ACS (2013). https://doi.org/10.1021/cg400645t
23. M. Bruzzi, C. Talamonti, N. Calisi, S. Caporali, A. Vinattieri, APL Mater. (2019). https://doi.org/10.1063/1.5083810
24. Q. Chen, J. Wu, X. Ou, B. Huang, J. Almutlaq, A.A. Zhumekenov, X. Guan, S. Han, L. Liang, Z. Yi, J. Li, X. Xie, Y. Wang, Y. Li, D. Fan, D.B.L. Teh, A.H. All, O.F. Mohammed, O.M. Bakr, T. Wu, M. Bettinelli, H. Yang, W. Huang, X. Liu, Nature (2018). https://doi.org/10.1038/s41586-018-0451-1
25. S. Hirotsu, J. Harada, M. Iizumi, K. Gesi, J. Phys. Soc. Jpn. (1974). https://doi.org/10.1143/JPSJ.37.1393
26. M. Rodová, J. Brožek, K. Knížek, K. Nitsch, J. Therm. Anal. Calorim. (2003). https://doi.org/10.1023/A:1022836800820
27. I.Y. Kuznetsova, I.S. Kovaleva, V.A. Fedorov, Zh. Neorg, Khim **34**, 1900 (2001)
28. S. Huang, Z. Li, B. Wang, N. Zhu, C. Zhang, L. Kong, Q. Zhang, A. Shan, L. Li, ACS Appl Mater. Interfaces (2017). https://doi.org/10.1021/acsami.6b14423
29. B. Kang, K. Biswas, J. Phys. Chem. Lett. (2018). https://doi.org/10.1021/acs.jpclett.7b03333
30. S. Seth, A. Samanta, J. Phys. Chem. Lett. (2017). https://doi.org/10.1021/acs.jpclett.7b02100
31. C. Rodà, A.L. Abdelhady, J. Shamsi, M. Lorenzon, V. Pinchetti, M. Gandini, F. Meinardi, L. Manna, S. Brovelli, Nanoscale (2019). https://doi.org/10.1039/C9NR01133A
32. C. Sun, Y. Zhang, C. Ruan, C. Yin, X. Wang, Y. Wang, W.W. Yu, Adv. Mater. (2016). https://doi.org/10.1002/adma.201603081
33. Z.J. Li, E. Hofman, J. Li, A.H. Davis, C.H. Tung, L.Z. Wu, W. Zheng, Adv. Funct. Mater. (2018). https://doi.org/10.1002/adfm.201704288
34. H. Guan, S. Zhao, H. Wang, D. Yan, M. Wang, Z. Zang, Nano Energy (2020). https://doi.org/10.1016/j.nanoen.2019.104279
35. H. Huang, B. Chen, Z. Wang, T.F. Hung, A.S. Susha, H. Zhong, A.L. Rogach, Chem. Sci. **7**, 5699 (2016)
36. Q. Zhou, Z. Bai, W.G. Lu, Y. Wang, B. Zou, H. Zhong, Adv. Mater. **28**, 9163 (2016)
37. S. Guarnera, A. Abate, W. Zhang, J.M. Foster, G. Richardson, A. Petrozza, H.J. Snaith, J. Phys. Chem. Lett. (2015). https://doi.org/10.1021/jz502703p
38. L. Xu, J. Li, T. Fang, Y. Zhao, S. Yuan, Y. Dong, J. Song, Nanoscale Adv. **1**, 980 (2019)

39. T.S. Montero, W. Soltanpoor, M. Morales-Masis, APL Mater. (2020). https://doi.org/10.1063/5.0027573
40. J. Li, X. Shan, S.G. Bade, T. Geske, Q. Jiang, X. Yang, Z. Yu, J. Phys. Chem. Lett. (2016). https://doi.org/10.1021/acs.jpclett.6b01942
41. M. Cesaria, M. Mazzeo, G. Quarta, M.R. Aziz, C. Nobile, S. Carallo, M. Martino, L. Calcagnile, A.P. Caricato, Nanomaterials (2021). https://doi.org/10.3390/nano11123210--
42. F. Palazon, Y. El Ajjouri, H.J. Bolink, Adv. Energy Mater. (2019). https://doi.org/10.1002/aenm.201902499
43. F. Palazon, Y. El Ajjouri, P. Sebastia-Luna, S. Lauciello, L. Manna, H.J. Bolink, J. Mater. Chem. C (2019). https://doi.org/10.1039/C9TC03778K
44. Q. Wang, B. Chen, Y. Liu, Y. Deng, Y. Bai, Q. Dong, J. Huang, Energy Environ. Sci. (2017). https://doi.org/10.1039/C6EE02941H
45. E.V. Péan, C.S.D. Castro, M.L. Davies, Mater. Lett. (2019). https://doi.org/10.1016/j.matlet.2019.01.103
46. H. Zhang, Y. Liu, H. Lu, W. Deng, K. Yang, Z. Deng, X. Zhang, S. Yuan, J. Wang, J. Niu, X. Zhang, Q. Jin, H. Feng, Y. Zhan, L. Zheng, Appl. Phys. Lett. (2017). https://doi.org/10.1063/1.5001843
47. Y. Wang, Y. Ren, S. Zhang, J. Wu, J. Song, X. Li, J. Xu, C.H. Sow, H. Zeng, H. Sun, Commun. Phys. (2018). https://doi.org/10.1038/s42005-018-0098-0
48. M. Lorenzon, L. Sortino, Q. Akkerman, S. Accornero, J. Pedrini, M. Prato, V. Pinchetti, F. Meinardi, L. Manna, S. Brovelli, Nano Lett. (2017). https://doi.org/10.1021/acs.nanolett.7b01253
49. R. Brenes, D. Guo, A. Osherov, N.K. Noel, C. Eames, E.M. Hutter, S.K. Pathak, F. Niroui, R.H. Friend, M.S. Islam, H.J. Snaith, V. Bulović, T.J. Savenije, S.D. Stranks, Joule (2017). https://doi.org/10.1016/j.joule.2017.08.006
50. J.M. Howard, E.M. Tennyson, S. Barik, R. Szostak, E. Waks, M.F. Toney, A.F. Nogueira, B.R.A. Neves, M.S. Leite, J. Phys. Chem. Lett. (2018). https://doi.org/10.1021/acs.jpclett.8b01357
51. D. Di Girolamo, M. Ibrahim-Dar, D. Dini, L. Gontrani, R. Caminiti, A. Mattoni, M. Graetzel, S. Meloni, J. Mater. Chem. A (2019). https://doi.org/10.1039/C9TA00715F
52. C.N.R. Rao, K. Biswas, *Essential of Inorganic Materials Synthesis* (Jhon Wiley & Sons Inc, Hoboken, 2015)
53. A. Jana, M. Mittal, A. Singla, S. Sapra, Chem. Commun (2017). https://doi.org/10.1039/C7CC00666G
54. Z.-Y. Zhu, Q.-Q. Yang, L.-F. Gao, L. Zhang, A.-Y. Shi, C.-L. Sun, Q. Wang, H.-L. Zhang, J. Phys. Chem. Lett (2017). https://doi.org/10.1021/acs.jpclett.7b00431
55. R.K. Singh, J. Narayan, J. Phys. Rev. B **41**, 8843 (1990)
56. N.J. Lanno, K.B. Erington, Rev. Sci. Instrum. (1992). https://doi.org/10.1063/1.1143762
57. L. Calcagnile, L. Maruccio, L. Scrimieri, D. Delle Side, E. Braione, M. D'Elia, G. Quarta, Nucl. Instrum. Methods Phys. Res. Sect. B (2019). https://doi.org/10.1016/j.nimb.2019.03.031
58. L. Calcagnile, G. Quarta, M. Elia, D. Muscogiuri, L. Maruccio, K. Butalag, G. Gianfrate, C. Sanapo, U. Toma, Nucl. Instrum. Methods Phys. Res. Sect. B (2005). https://doi.org/10.1016/j.nimb.2005.06.081
59. D. Chirizzi, D. Mastrogiacomo, P. Semeraro, F. Milano, A.R. De Bartolomeo, M. Trotta, L. Valli, L. Giotta, M. R. Guascito, Appl. Surface Sci. **593**, 153385 (2022)
60. D. Briggs, M.P. Seah (eds.), *Practical Surface Analysis by Auger and X-Ray Photoelectron Spectroscopy*, 2nd edn. (Wiley, Chichester, 1990)
61. J. Lei, F. Gao, H. Wang, J. Li, J. Jiang, X. Wu, R. Gao, Z. Yang, S. Liu, Sol. Energy Mater. Sol. Cells (2018). https://doi.org/10.1016/j.solmat.2018.07.009
62. R.J. Sutton, E.E. Giles, L. Miranda, E.S. Parrott, B.A. Kamino, J.B. Patel, M.T. Horantner, M.B. Johnston, A.A. Haghighirad, D.T. Moore, H.J. Snaith, Adv. Energy Mater. (2016). https://doi.org/10.1002/aenm.201502458
63. M. Nikl, E. Mihóková, K. Nitsch, F. Somma, C. Giampaolo, G. Pazzi, P. Fabeni, S. Zazubovich, Phys. Lett. (1999). https://doi.org/10.1016/S0009-2614(99)00477-7
64. Q. Jing, Y. Xu, Y. Su, X. Xing, Z. Lu, Nanoscale (2019). https://doi.org/10.1039/C8NR08116F
65. H.-R. Kim, J.-H. Bong, J.-H. Park, Z. Song, M.-J. Kang, D.H. Son, J.-C. Pyun, ACS Appl. Mater. Interfaces (2021). https://doi.org/10.1021/acsami.1c08128
66. S.-C. Liu, Z. Li, Y. Yang, X. Wang, Y.-X. Chen, D.-J. Xue, J.-S. Hu, J. Am. Chem. Soc. (2019). https://doi.org/10.1021/jacs.9b07182
67. J.S.W. Godding, A.J. Ramadan, Y.-H. Lin, K. Schutt, H.J. Snaith, B. Wenger, Joule (2019). https://doi.org/10.1016/j.joule.2019.08.006
68. M. Shin, H.S. Lee, Y.C. Sim, Y.-H. Cho, K.C. Choi, B. Shin, A.C.S. Appl, Mater. Interfaces (2020). https://doi.org/10.1021/acsami.9b20094
69. Q.A. Akkerman, V. D'Innocenzo, S. Accornero, A. Scarpellini, A. Petrozza, M. Prato, L. Manna, J. Am. Chem. Soc. (2015). https://doi.org/10.1021/jacs.5b05602
70. S. Kondo, K. Amaya, T. Saito, J. Phys. Condens. Matter **14**, 2093 (2002)
71. M. Kulbak, D. Cahen, G. Hodes, J. Phys. Chem. Lett. (2015). https://doi.org/10.1021/acs.jpclett.5b00968
72. L. Nasi, D. Calestani, F. Mezzadri, F. Mariano, A. Listorti, P. Ferro, M. Mazzeo, R. Mosca, Front. Chem. (2020). https://doi.org/10.3389/fchem.2020.00313